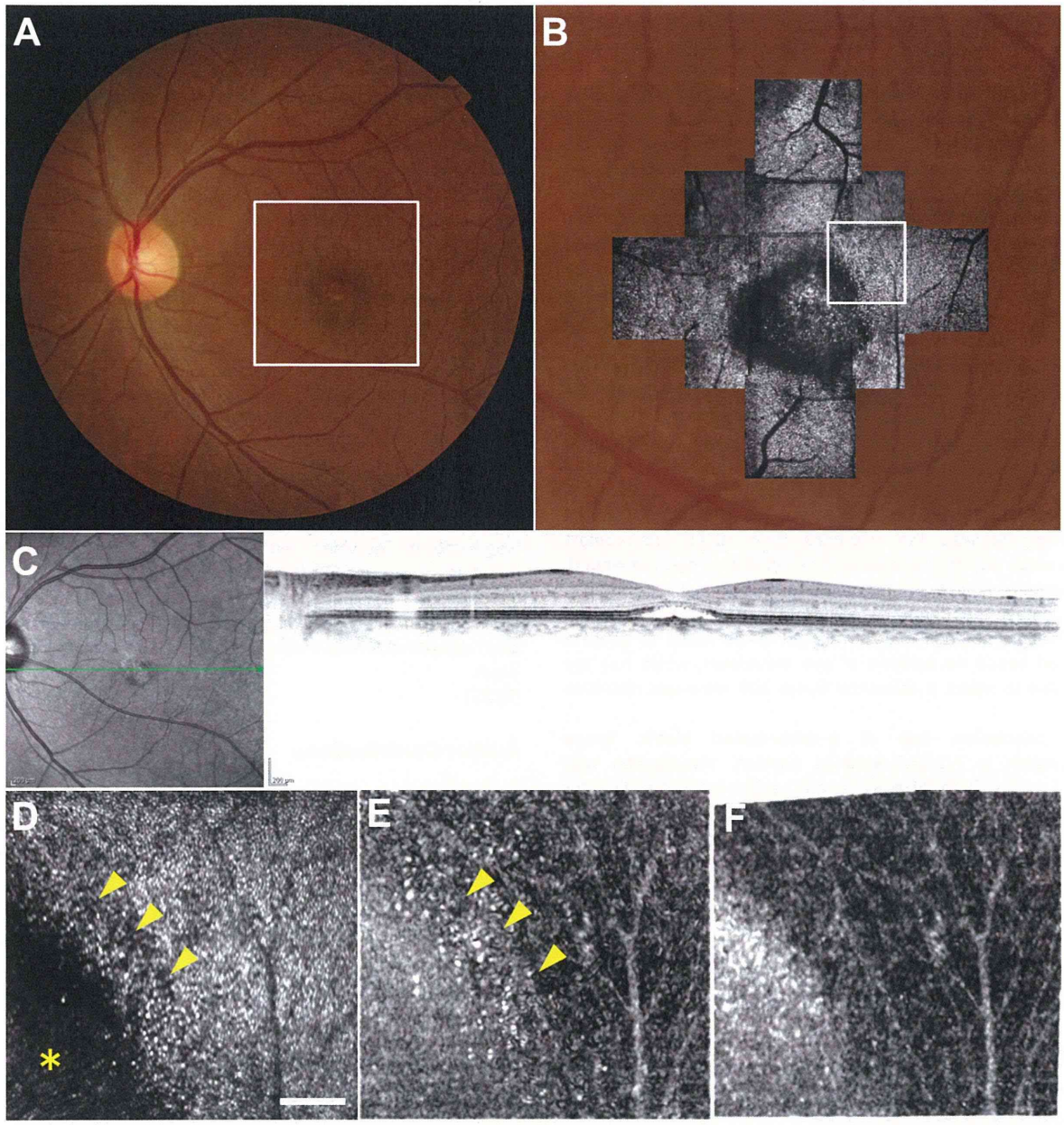

Figure 8. Imaging Results from Case 5. (A) Color fundus photograph. (B) Montage of adaptive optics scanning laser ophthalmoscopy (AO-SLO) images overlaid on magnified color fundus photograph corresponding to the area outlined in white in (A). (C) The optical coherence tomographic scan shows serous retinal detachment and irregularity of the retinal pigment epithelium at the fovea. (D) First frame of the AO-SLO video, which corresponds to the area outlined in white in (B). A dark area is noted on the fovea (asterisk), and many dark patches (arrowheads) representing lost or damaged cones are detected around the dark area. Vessel shadows near the fovea assimilated into the dark area and were not visible. Scale bar, 100 μm. (E) Capillary image constructed from unregistered AO-SLO video. A spotty area was seen in the region containing dark patches (arrowheads). These spots may be due to imperfect alignment. (F) Capillary image constructed from AO-SLO video after B-spline-based elastic registration. The spotty area seen in (E) is not detected.

doi: 10.1371/journal.pone.0080106.g008

from photoreceptors are affected by blood cells because of their different scattering coefficients[43]. When the scanning is focused on the photoreceptor layer, leukocytes and blood plasma are candidates for the bright particles moving in the dark vessel shadows due to the low absorptivity of the AO-SLO laser, and erythrocytes are candidates for the region that is darker than the vessel shadow because they block the AO-SLO lasers. Accordingly, the presence of structures that can block the laser or absences of photoreceptors that can reflect the laser as in the case of microfolds and loss of cone mosaic pattern will lead to the failure of blood flow detection. Although a possible solution to the problem may be focusing the scanning layer on the capillary layer, further investigation is needed to assess the optimal focus for capillary visualization using AO-SLO.

Our study has several limitations: (1) Because the registration was computed after video recording without real time eye-tracking, video recording was limited to a short duration to minimize the inter-frame position gap between scan frames. Longer-duration video recording may fail to construct adequately wide-area capillary images (2). The first frame of the video was used as a fixed reference frame for image warping. Because the reference frame itself can contain substantial distortions produced by intraframe eye movement, subsequent source frames and constructed capillary images will contain the same distortions. To overcome this issue, registration methods may be altered in the future to adopt a method based on analysis of eye movement, which has the potential to select a reference frame with minimum distortion [44].

In conclusion, use of B-spline-based elastic image registration in AO-SLO-assisted capillary visualization was found to be both objectively and subjectively effective for enhancing image quality. Its high-quality interpolation and ready availability may further facilitate the application of AO-SLO for the study of retinal microcirculation.

Supporting Information

Digital Content S1. Detailed description of the algorithm of bUnwarpJ Developed as an ImageJ Plug-in.
(DOCX)

Digital Content S2. Macro for Continuous Elastic Image Registration Using bUnwarpJ Developed as an ImageJ Plug-in. Before elastic image registration, videos were cropped to eliminate the margin without retinal image, which was a by-product of registration. Our macro was programmed to use the first frame as a fixed reference frame for image warping by bUnwarpJ. Note that the advanced setting of bUnwarpJ was modified to function successfully in our AO-SLO images.
(TIF)

Digital Content S3. Macro for Capillary Visualization. The capillary images were constructed as projections of the moving objects in sequential frames using the motion contrast enhancement with this macro. In accordance with the total frame number of the video, the original data for frame number, indicated as 64 on the second line and the fifth line from the top, need to be rewritten.
(TIF)

Digital Content S4. Movies with and without Elastic Image Registration. The video field size is 674 × 705 μm^2 each, and the frame rate is 32 fps. Distortion that was wavy and uncorrectable by linear image registration was considerably diminished in the video with elastic image registration (right side) compared to video without elastic image registration (Left Side).
(MOV)

Author Contributions

Conceived and designed the experiments: AU SO. Performed the experiments: AU SA. Analyzed the data: AU SO MH. Contributed reagents/materials/analysis tools: AU SA. Wrote the manuscript: AU SO MH SA NY.

References

1. Huang D, Swanson EA, Lin CP, Schuman JS, Stinson WG et al. (1991) Optical coherence tomography. Science 254: 1178-1181. doi:10.1126/science.1957169. PubMed: 1957169.
2. Gupta V, Gupta P, Singh R, Dogra MR, Gupta A (2008) Spectral-domain Cirrus high-definition optical coherence tomography is better than time-domain Stratus optical coherence tomography for evaluation of macular pathologic features in uveitis. Am J Ophthalmol 145: 1018-1022. doi:10.1016/j.ajo.2008.01.021. PubMed: 18343349.
3. Chang RT, Knight OJ, Feuer WJ, Budenz DL (2009) Sensitivity and specificity of time-domain versus spectral-domain optical coherence tomography in diagnosing early to moderate glaucoma. Ophthalmology 116: 2294-2299. doi:10.1016/j.ophtha.2009.06.012. PubMed: 19800694.
4. Forooghian F, Cukras C, Meyerle CB, Chew EY, Wong WT (2008) Evaluation of time domain and spectral domain optical coherence tomography in the measurement of diabetic macular edema. Invest Ophthalmol Vis Sci 49: 4290-4296. doi:10.1167/iovs.08-2113. PubMed: 18515567.
5. Kim JS, Ishikawa H, Gabriele ML, Wollstein G, Bilonick RA et al. (2010) Retinal nerve fiber layer thickness measurement comparability between time domain optical coherence tomography (OCT) and spectral domain OCT. Invest Ophthalmol Vis Sci 51: 896-902. doi:10.1167/iovs.09-4110. PubMed: 19737886.
6. Uji A, Murakami T, Nishijima K, Akagi T, Horii T et al. (2012) Association between hyperreflective foci in the outer retina, status of photoreceptor layer, and visual acuity in diabetic macular edema. Am J Ophthalmol 153: 710-717 doi:10.1016/j.ajo.2011.08.041. PubMed: 22137207.
7. Yamaike N, Tsujikawa A, Ota M, Sakamoto A, Kotera Y et al. (2008) Three-dimensional imaging of cystoid macular edema in retinal vein occlusion. Ophthalmology 115: 355-362. doi:10.1016/j.ophtha.2007.04.052. PubMed: 17675242.
8. Sakamoto A, Hangai M, Yoshimura N (2008) Spectral-domain optical coherence tomography with multiple B-scan averaging for enhanced imaging of retinal diseases. Ophthalmology 115: 1071-1078 . doi: 10.1016/j.ophtha.2007.09.001. PubMed: 18061270.

9. Hangai M, Yamamoto M, Sakamoto A, Yoshimura N (2009) Ultrahigh-resolution versus speckle noise-reduction in spectral-domain optical coherence tomography. Opt Express 17: 4221-4235. doi:10.1364/OE.17.004221. PubMed: 19259257.
10. Roorda A, Romero-Borja F, Donnelly Iii , Queener H, Hebert T et al. (2002) Adaptive optics scanning laser ophthalmoscopy. Opt Express 10: 405-412. doi:10.1364/OE.10.000405. PubMed: 19436374.
11. Martin JA, Roorda A (2005) Direct and noninvasive assessment of parafoveal capillary leukocyte velocity. Ophthalmology 112: 2219-2224. doi:10.1016/j.ophtha.2005.06.033. PubMed: 16257054.
12. Tam J, Tiruveedhula P, Roorda A (2011) Characterization of single-file flow through human retinal parafoveal capillaries using an adaptive optics scanning laser ophthalmoscope Biomed Opt Express 2: 781-793. PubMed: 21483603.
13. Vogel CR, Arathorn DW, Roorda A, Parker A (2006) Retinal motion estimation in adaptive optics scanning laser ophthalmoscopy. Opt Express 14: 487-497. doi:10.1364/OPEX.14.000487. PubMed: 19503363.
14. Li H, Lu J, Shi G, Zhang Y (2010) Tracking features in retinal images of adaptive optics confocal scanning laser ophthalmoscope using KLT-SIFT algorithm Biomed Opt Express 1: 31-40. PubMed: 21258443.
15. Merino D, Duncan JL, Tiruveedhula P, Roorda A (2011) Observation of cone and rod photoreceptors in normal subjects and patients using a new generation adaptive optics scanning laser ophthalmoscope. Biomedical. Opt Express 2: 2189-2201. doi:10.1364/BOE.2.002189.
16. Sheehy CK, Yang Q, Arathorn DW, Tiruveedhula P, de Boer JF et al. (2012) High-speed, image-based eye tracking with a scanning laser ophthalmoscope Biomed Opt Express 3: 2611-2622. PubMed: 23082300.
17. Arathorn DW, Yang Q, Vogel CR, Zhang Y, Tiruveedhula P et al. (2007) Retinally stabilized cone-targeted stimulus delivery. Opt Express 15: 13731-13744. doi:10.1364/OE.15.013731. PubMed: 19550644.
18. Yang Q, Arathorn DW, Tiruveedhula P, Vogel CR, Roorda A (2010) Design of an integrated hardware interface for AOSLO image capture and cone-targeted stimulus delivery. Opt Express 18: 17841-17858. doi:10.1364/OE.18.017841. PubMed: 20721171.
19. Martin JA, Roorda A (2009) Pulsatility of parafoveal capillary leukocytes. Exp Eye Res 88: 356-360. doi:10.1016/j.exer.2008.07.008. PubMed: 18708051.
20. Tam J, Martin JA, Roorda A (2010) Noninvasive visualization and analysis of parafoveal capillaries in humans. Invest Ophthalmol Vis Sci 51: 1691-1698. doi:10.1167/iovs.09-4483. PubMed: 19907024.
21. Tam J, Dhamdhere KP, Tiruveedhula P, Manzanera S, Barez S et al. (2011) Disruption of the retinal parafoveal capillary network in type 2 diabetes before the onset of diabetic retinopathy. Invest Ophthalmol Vis Sci 52: 9257-9266. doi:10.1167/iovs.11-8481. PubMed: 22039250.
22. Tam J, Dhamdhere KP, Tiruveedhula P, Lujan BJ, Johnson RN et al. (2012) Subclinical capillary changes in non-proliferative diabetic retinopathy. Optom Vis Sci 89: E692-E703. doi:10.1097/OPX.0b013e3182548b07. PubMed: 22525131.
23. Chiang P, Cai Y, Mak KH, Zheng J (2012) A B-spline approach to phase unwrapping in tagged cardiac MRI for motion tracking. Magn Reson Med.
24. Feng W, Reeves SJ, Denney TS, Lloyd S, Dell'Italia L et al. (2009) A New Consistent Image Registration Formulation with a B-Spline Deformation Model. 2009 Ieee International Symposium on Biomedical Imaging: From Nano to Macro, Vols 1 and 2: 979-982
25. Lee ETY (1982) A Simplified B-Spline Computation Routine. Computing 29: 365-371. doi:10.1007/BF02246763.
26. Oguro S, Tokuda J, Elhawary H, Haker S, Kikinis R et al. (2009) MRI signal intensity based B-spline nonrigid registration for pre- and intraoperative imaging during prostate brachytherapy. J Magn Reson Imaging 30: 1052-1058. doi:10.1002/jmri.21955. PubMed: 19856437.
27. Rogers JM (2000) Modeling the cardiac action potential using B-spline surfaces. IEEE Trans Biomed Eng 47: 784-791. doi: 10.1109/10.844229. PubMed: 10833853.
28. Hirose F, Nozato K, Saito K, Numajiri Y (2011) A compact adaptive optics scanning laser ophthalmoscope with high-efficiency wavefront correction using dual liquid crystal on silicon - spatial light modulator. Proc of SPIE.
29. Lasers ANSftSUo (2007) ANSI Z136.1-2007. New York: American National Standards Institute.
30. Uji A, Hangai M, Ooto S, Takayama K, Arakawa N et al. (2012) The source of moving particles in parafoveal capillaries detected by adaptive optics scanning laser ophthalmoscopy. Invest Ophthalmol Vis Sci 53: 171-178. doi:10.1167/iovs.11-8192. PubMed: 22159004.
31. Thévenaz P, Ruttimann UE, Unser M (1998) A pyramid approach to subpixel registration based on intensity. IEEE Trans Image Process 7: 27-41. doi:10.1109/83.650848. PubMed: 18267377.
32. Arganda-Carreras I, Sorzano C, Marabini R, Carazo J, Ortiz-De-Solorzano C et al. (2006) Consistent and Elastic Registration of Histological Sections using Vector-Spline Regularization. Berlin / Heidelberg: Springer Verlag.
33. Sorzano CO, Thévenaz P, Unser M (2005) Elastic registration of biological images using vector-spline regularization. IEEE Trans Biomed Eng 52: 652-663. doi:10.1109/TBME.2005.844030. PubMed: 15825867.
34. Stetson PF, Sommer FG, Macovski A (1997) Lesion contrast enhancement in medical ultrasound imaging. IEEE Trans Med Imaging 16: 416-425. doi:10.1109/42.611351. PubMed: 9262999.
35. Takayama K, Ooto S, Hangai M, Arakawa N, Oshima S et al. (2012) High-resolution imaging of the retinal nerve fiber layer in normal eyes using adaptive optics scanning laser ophthalmoscopy. PLOS ONE 7: e33158. doi:10.1371/journal.pone.0033158. PubMed: 22427978.
36. Takayama K, Ooto S, Tamura H, Yamashiro K, Otani A et al. (2010) Intravitreal bevacizumab for type 1 idiopathic macular telangiectasia. Eye (Lond) 24: 1492-1497. doi:10.1038/eye.2010.61. PubMed: 20431610.
37. Yannuzzi LA, Bardal AM, Freund KB, Chen KJ, Eandi CM et al. (2006) Idiopathic macular telangiectasia. Arch Ophthalmol 124: 450-460. doi: 10.1001/archopht.124.4.450. PubMed: 16606869.
38. Ooto S, Hangai M, Takayama K, Sakamoto A, Tsujikawa A et al. (2011) High-resolution imaging of the photoreceptor layer in epiretinal membrane using adaptive optics scanning laser ophthalmoscopy. Ophthalmology 118: 873-881. doi:10.1016/j.ophtha.2010.08.032. PubMed: 21074858.
39. Ooto S, Hangai M, Sakamoto A, Tsujikawa A, Yamashiro K et al. (2010) High-resolution imaging of resolved central serous chorioretinopathy using adaptive optics scanning laser ophthalmoscopy. Ophthalmology 117: 1800-1809 doi:10.1016/j.ophtha.2010.01.042. PubMed: 20673590.
40. Deng X, Denney TS Jr. (2004) Three-dimensional myocardial strain reconstruction from tagged MRI using a cylindrical B-spline model. IEEE Trans Med Imaging 23: 861-867. doi:10.1109/TMI.2004.827961. PubMed: 15250638.
41. Lowe DG (2004) Distinctive image features from scale-invariant keypoints. Int J Comput Vis 60: 91-110. doi:10.1023/B:VISI.0000029664.99615.94.
42. Shi JB, Tomasi C (1994) Good Features to Track. 1994 Ieee Computer Society Conference on Computer Vision and Pattern Recognition, Proceedings: 593-600.
43. Meinke M, Müller G, Helfmann J, Friebel M (2007) Optical properties of platelets and blood plasma and their influence on the optical behavior of whole blood in the visible to near infrared wavelength range. J Biomed Opt 12: 014024. doi:10.1117/1.2435177. PubMed: 17343499.
44. Dubra A, Harvey Z (2010) Registration of 2D Images from Fast Scanning Ophthalmic Instruments. Biomedical Images Registration 6204: 60-71. doi:10.1007/978-3-642-14366-3_6.

Noninvasive and Direct Monitoring of Erythrocyte Aggregates in Human Retinal Microvasculature Using Adaptive Optics Scanning Laser Ophthalmoscopy

Shigeta Arichika, Akihito Uji, Masanori Hangai, Sotaro Ooto, and Nagahisa Yoshimura

Department of Ophthalmology and Visual Sciences, Kyoto University Graduate School of Medicine, Kyoto, Japan

Correspondence: Akihito Uji, Department of Ophthalmology and Visual Sciences, Kyoto University Graduate School of Medicine, 54 Shogoin Kawahara-cho, Shougoin, Sakyo-ku, Kyoto 606-8507, Japan; akihito1@kuhp.kyoto-u.ac.jp.

Submitted: October 13, 2012
Accepted: May 18, 2013

Citation: Arichika S, Uji A, Hangai M, Ooto S, Yoshimura N. Noninvasive and direct monitoring of erythrocyte aggregates in human retinal microvasculature using adaptive optics scanning laser ophthalmoscopy. *Invest Ophthalmol Vis Sci.* 2013;54:4394-4402. DOI:10.1167/iovs.12-11138

Purpose. To investigate erythrocyte aggregates in parafoveal capillaries by adaptive optics scanning laser ophthalmoscopy (AO-SLO).

Methods. AO-SLO videos were acquired from the parafoveal areas of one eye in 10 healthy subjects. Erythrocyte aggregates were detected as "dark tails" that were darker regions than vessel shadows. The lengths of the dark tails were measured in target capillaries, and their time-dependent changes in length were analyzed using spatiotemporal images. The dark tail elongation rate was calculated as the change of dark tail length per unit length of the target capillary.

Results. The overall average dark tail length was 112.1 ± 36.9 μm. The dark tail became longer in a time-dependent manner in every monitored capillary ($P < 0.0001$). The dark tail elongation rate and average velocity were 0.51 ± 0.37 and 1.49 ± 0.36 mm/s, respectively.

Conclusions. AO-SLO can be used for noninvasive and direct monitoring of blood dynamics in the retinal microvasculature without dying agents. Erythrocyte aggregates were detected as dark tails and were elongated in a time-dependent manner in the parafoveal capillaries of normal subjects. Monitoring the characteristics of dark tails has promising potential for evaluating retinal hemodynamics.

Keywords: AO-SLO, erythrocyte aggregates, blood flow, dark tail, parafoveal capillary

Retinal vessels can be observed directly through the window of the pupils. Information regarding abnormalities and diseases related to circulation are often first revealed by the observation of retinal vessels, which leads to speedy and appropriate treatment for patients.[1] The appearance of vessels contributes to the grading of noteworthy systemic disorders such as hypertension,[2,3] arteriosclerosis, and diabetic retinopathy.[1,4] Furthermore, investigating hemodynamics in the human retina provides potentially helpful information and clues for understanding the pathogenesis of retinal vascular disorders such as diabetic retinopathy,[5] glaucoma,[6] age-related macular degeneration,[7] retinal vein occlusion,[8] and collagen diseases.[9]

Many approaches have been developed for evaluating blood vessels or dynamic blood flow, including the dye dilution technique,[10–12] blue field entoptic phenomenon,[13–15] laser Doppler velocimetry,[16–19] laser speckle phenomenon,[20] optical coherence tomography (OCT),[21] and adaptive optics scanning laser ophthalmoscopy (AO-SLO).[22–25] These techniques, except for blue field entoptic phenomenon and AO-SLO, evaluate the blood flow in the retina but do not monitor the blood corpuscles in the retinal capillary.

Many reports have described erythrocyte dynamics in animal studies and ex vivo capillary models and simulation.[26–29] Erythrocyte behaviors such as aggregations, deformations, or abnormalities change in response to vascular status or the presence of diseases like sickle-cell anemia,[30] diabetes mellitus,[31] systemic lupus erythematosus (SLE),[9] or Behçet's disease.[32] Meanwhile, few reports have described erythrocyte aggregations in the human eye with the exception of the conjunctiva bulbi.[33] An in vivo approach for monitoring erythrocyte aggregates directly in the retinal microcirculation has not been reported.

Recently, confocal AO-SLO has enabled imaging of retinal cells such as photoreceptors and leukocytes.[5,24,34,35] AO-SLO is a SLO-equipped adaptive optics technology that provides high-resolution and high-contrast retinal images by correcting ocular aberrations.[36,37] AO-SLO images allow the noninvasive monitoring of leukocyte movements as bright particles flowing in dark parafoveal capillaries and the measurement of their velocities without the use of contrast dyes.[10–12] We previously reported that the bright particles moving in the dark vessel shadows may be reflections of the photoreceptor aggregates that pass through circulating transparent objects such as leukocytes or plasma gaps. Furthermore, we described the so-called dark tail, which could be seen as a region darker than the vessel shadow that occurred closely behind moving particles and might correspond to aggregated erythrocytes upstream of the leukocytes that block the AO-SLO laser (Fig. 1A).[24]

In this study, we performed direct, noninvasive, and objective quantification of the "dark tail" in the parafoveal capillaries of healthy human eyes by using our AO-SLO system.

Methods

This study was approved by the Institutional Review Board and the Ethics Committee at Kyoto University Graduate School of Medicine and was performed in accordance with the tenets of the Declaration of Helsinki. Written informed consent was

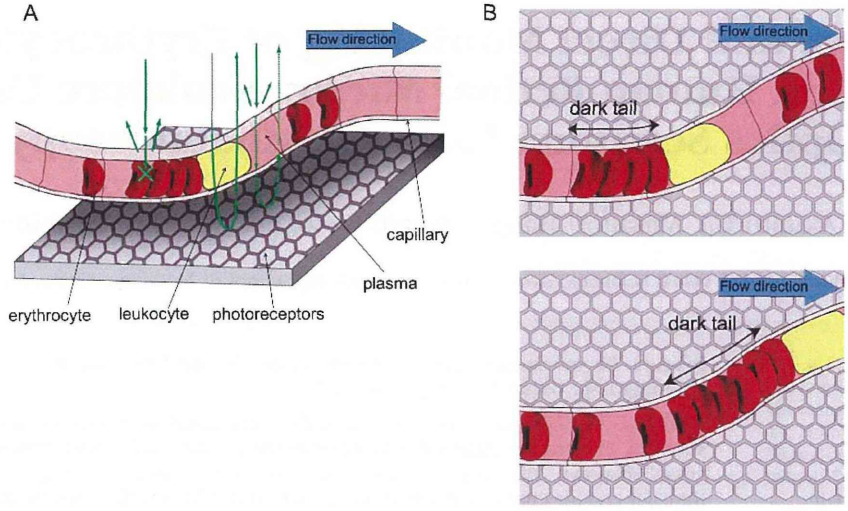

FIGURE 1. Schema of dark tail elongation in the parafoveal capillary. (**A**) Diagrammatic representation of the optical properties of blood plasma and blood cells in the parafoveal capillaries. The adaptive optics scanning laser ophthalmoscopy (AO-SLO) laser passes through leukocytes, and the reflective light from photoreceptors (*hexagons*) enables leukocytes to be detected as bright moving objects when the scanning layer is focused on the photoreceptor layer. Erythrocyte aggregates prevent the AO-SLO laser from reaching the photoreceptor and are detected as dark shadows on the photoreceptor layer (dark tail). Blood cells flow in single file in the capillary lumen, and the dark tail follows closely behind the slow-moving leukocytes. (**B**) Leukocytes interfere with the flow of erythrocyte aggregates and cause the erythrocytes to become packed together sequentially, resulting in the detection of an elongated dark tail closely behind leukocytes in AO-SLO videos.

obtained from each participant after a detailed explanation of the nature and possible consequences of the study procedures.

Subjects

AO-SLO videos were acquired from the parafoveal areas of 10 healthy Japanese subjects (mean age ± standard deviation [SD], 32.6 ± 6.7 years; range, 22–42 years) without a history of ocular or systemic diseases. All subjects were dilated before imaging with one set of tropicamide (0.5%) and phenylephrine hydrochloride (0.5%) drops and were examined for approximately 10 minutes per eye in a seated posture.

Adaptive Optics Scanning Laser Ophthalmoscopy Imaging

We developed a novel AO-SLO system (Canon, Inc., Tokyo, Japan) with a high wavefront correction efficiency using a dual liquid-crystal phase modulator (LCOS-SLM; X10468-02; Hamamatsu Photonics, Hamamatsu, Japan), as described previously (Fig. 2).[38] Briefly, the imaging wavelength was 840 ± 25 nm, and the wavelength of beacon light for the measurement of wavefront aberrations was 760 ± 5 nm. The imaging light and the beacon light were set at 330 and 40 μW, respectively, by calculating the incident power of both light sources in accordance with the safety limits set by the American National Standards Institute.[39] The videos were acquired at 64 frames/s. The scan area was 1.4 × 2.8° at the retina and was sampled at 200 × 400 pixels.

Video Processing

Desinusoiding. We calculated each pixel value of the AO-SLO image from the intensity of the reflective light measured at regular time intervals. The resonant scanner changes its scan speed sinusoidally, and the AO-SLO obtains the intensity of the reflective light at regular time intervals. Therefore, it obtains a few intensity values near the center and many intensity values near edge of the image.

In this study, we presumed that the AO-SLO image was composed of the intensity of the reflective light from the imaging light that is scanned on the retina with the scanner.

Each pixel value of the AO-SLO image was calculated using the weighted mean method based on the time for which the imaging light was scanned on the retina, under the assumption that its scan speed changed sinusoidally.

Video Stabilization. Raw videos were corrected for scanning distortions and were stabilized to correct for eye motion by using ARIA (AO-SLO Retinal Image Analyzer; Canon, Inc.). The registration technique of ARIA is based on scan line warping, and a fixed reference frame is used for image warping.[24,40]

AO-SLO Movie Acquisition

AO-SLO videos were recorded for 4 seconds per scan area, and 10 to 25 scan areas were collected per subject to cover the parafoveal areas. AO-SLO imaging was performed by focusing on the photoreceptor layer to enable detection of the cone mosaic pattern.

Quantitative Image Analysis of the Dark Tail

The dark tail was defined as a region darker than the vessel shadow that occurred closely behind the moving bright particles (Fig. 1B). In this study, we investigated the dark tail as a shadow of aggregated erythrocytes that blocked the AO-SLO laser. All digital images, except for video stabilization and capillary visualization, were processed by a single operator (SA) using the public-domain software ImageJ (available in the public domain at http://rsb.info.nih.gov/ij/index.html; developed by Wayne Rasband, National Institutes of Health, Bethesda, MD). The grayscale ranged from 0 (black) to 255 (white).

Capillary Visualization. The capillary images were constructed as projections of the moving objects in sequential frames by using the motion contrast-enhancement technique, which was first introduced by Tam et al. as an image

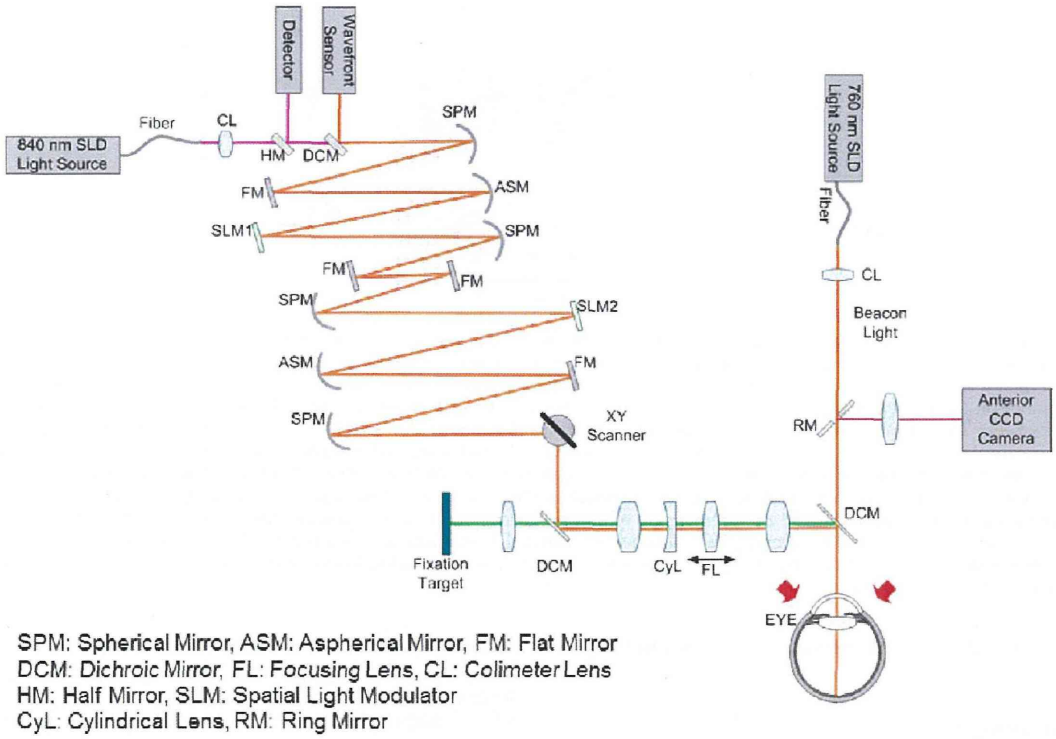

FIGURE 2. Schematic of the optical structure of AO-SLO. Two spatial light modulators (SLM) are used for wavefront correction, and the cylindrical lens (CyL) is used to compensate for the large astigmatism of eyes. The aspherical mirror is used to compensate for the aberration from the off-axis layout mirrors. The two *red arrows* represent the infrared light used to observe eye fixation.

processing technique for capillary visualization using AO-SLO videos.[41,42] In brief, motion contrast enhancement was conducted by dividing the pixels between sequential frames followed by calculating the variance of pixels among all division images in each X–Y position, resulting in visualization of the contrast-enhanced capillary images. Visualized vessels were used for the following analyses to set the regions of interest (ROI) along the target vessels precisely. All digital image processing for capillary visualization was manipulated by ARIA automatically.

Velocity Measurement of the Dark Tail. The target vessels with dark tail flow were selected from one branch to another to ensure that they were free of another bifurcation. The dark tail velocity was calculated by using a spatiotemporal image generated by reslicing the sequential frames, with the length of the line on the horizontal axis and the frame number on the vertical axis.[24,43] After reslicing of the frames along the line set on the target vessel (Fig. 3A), the velocity was obtained by calculating the reciprocal of the slope of the borderline between the white band and black band depicted in the spatiotemporal image, which correspond to the loci of moving bright particles and the dark tail, respectively (Fig. 3B). A steeper slope indicates a lower velocity. We measured three individual capillaries per subject, which were selected randomly. The velocities of three individual successive dark tails were measured for each capillary, yielding 90 measurements.

Measurement of Dark Tail Length. Dark tail length was calculated by using a spatiotemporal image in which the dark tail velocities and the time required for the dark tail to pass the points on the target vessel could be seen simultaneously. First, a straight vertical line was set on the spatiotemporal image and a plot profile was prepared. The frame number of the gray value range that was lower than the background gray value was measured as the time required for the dark tail to pass the point on the target vessel (Figs. 3B, 3C). The background gray value was defined as the average gray value of a region free of dark tails and bright moving objects such as leukocytes or plasma gaps. Together with the velocity of the dark tail mentioned above, the dark tail length was calculated as follows:

$$l = v \times t, \tag{1}$$

where l and v are the length and velocity of the dark tail, respectively, and t is the time required for the dark tail to pass through a point located on the target vessel. In addition, the spatiotemporal image was separated vertically into three zones from upstream to downstream of the blood flow (zones a, b, and c), and the dark tail length was calculated for each zone to evaluate time-dependent dark tail changes. The dark tail elongation rate was defined as follows:

$$r = \frac{l_c - l_a}{L}, \tag{2}$$

where r, L, l_c, and l_a are the elongation rate, the distance between zone a and zone c, the dark tail length at zone c, and the dark tail length at zone a, respectively. We measured three individual and randomly selected capillaries in each subject. The length of three individual dark tails was measured for each capillary, yielding a total of 270 measurements.

Capillary Diameter Measurement

Capillary diameters were measured to evaluate the association with the elongation rate of the dark tail. The parafoveal capillary diameters were measured on the constructed

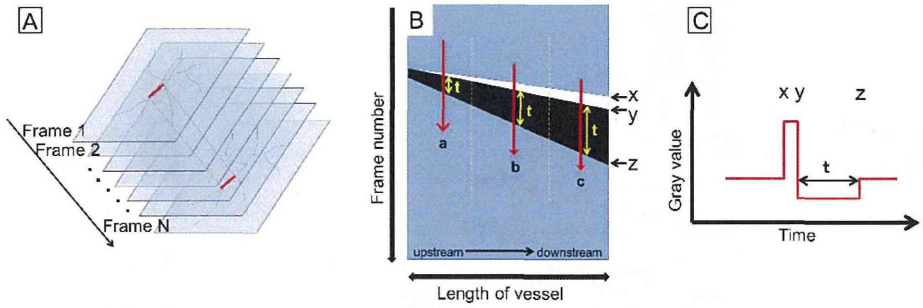

FIGURE 3. Measurement of dark tail velocity and length using a spatiotemporal image. (**A**) Schema of stacked sequential AO-SLO images. *Red lines* are focused on the target vessel in preparation for reslicing of the sequential images in order to generate the spatiotemporal image. (**B**) The dark tail velocity and length were calculated by using a spatiotemporal image that was plotted with the length of the target vessel on the horizontal axis and the frame number on the vertical axis. The *white narrow band* and the *wider black band* represent the trajectory of bright moving objects and dark tail, respectively. The thickness of the black band (t) represents the time required for the dark tail to pass through a point located on the target vessel. The reciprocal of the slope of the borderline between the white and black bands represents the velocity of the head of the dark tail. The spatiotemporal image was vertically separated into three zones from upstream to downstream of the blood flow (zones a, b, and c), and the dark tail length was calculated for each zone to evaluate the time-dependent changes in the dark tails. (**C**) Plot profile of the *red line* set on the spatiotemporal image in (**B**). Points x, y, and z and the length of time (t) correspond to x, y, z, and t in (**B**), respectively. The frame number of the gray value range that was lower than the averaged gray value was measured as the time required for the dark tail to pass the point on the target vessel. The dark tail length was computed by multiplying the velocity by the time. Dark tail velocities were calculated for each zone to evaluate the time-dependent changes in dark tails.

capillary images and were measured for each of the three zones manually.

Statistical Analysis

All values are presented as the mean ± SD. The statistically significant correlations between the elongation rate and velocity, between the elongation rate and diameter, between the velocity and diameter, and between the length of the dark tail and diameter were evaluated with the Pearson's correlation coefficient. The differences in dark tail length and capillary diameter among the three zones were evaluated with analysis of variance (ANOVA) followed by repeated measures ANOVA. All calculations were performed using StatView (version 5.0; SAS, Inc., Cary, NC) except for the intraclass correlation coefficient (ICC), which was calculated using SPSS (IBM SPSS statistics 19; IBM, Inc., Armonk, NY). P values less than 0.05 were considered significant.

RESULTS

Appearance of the Dark Tail

By using our prototype AO-SLO, we successfully captured bright moving objects and dark tails flowing in parafoveal capillaries in all subjects, as previously reported.[24] All dark tails were observed as black "tadpole tail"-like regions that were darker than the vessel shadow, following closely after the bright moving objects that were previously reported as leukocytes or plasma gaps (Fig. 4 and Supplementary Movie S1).[24] Although dark tails were detected in parafoveal capillaries, they were not detected in larger vessels such as the terminal artery or collecting venules. Moreover, dark tails were not detected in all of the capillaries, and they appeared to flow in a fixed path. They suddenly appeared at a branch of the parafoveal capillary, flowed in the capillary network, and disappeared when they reached the larger vessels.

Dark Tail Velocity

The average velocity of the dark tails of normal subjects was 1.49 ± 0.36 mm/s, with a range of 0.79 to 2.19 mm/s (Table).

Dark Tail Length

The lengths of the dark tails were calculated successfully in all subjects by using spatiotemporal images acquired from target vessels (Fig. 5). Examples of spatiotemporal images are shown in Figure 6. All examples show several dark bands that corresponded to the trajectories of the dark tails and were narrowest upstream and broadest downstream, indicating gradual elongation of the dark tails. The overall average length of the dark tails was 112.1 ± 36.9 μm, with a range of 21.1 to 302.2 μm. The average lengths of the dark tails at zones a, b,

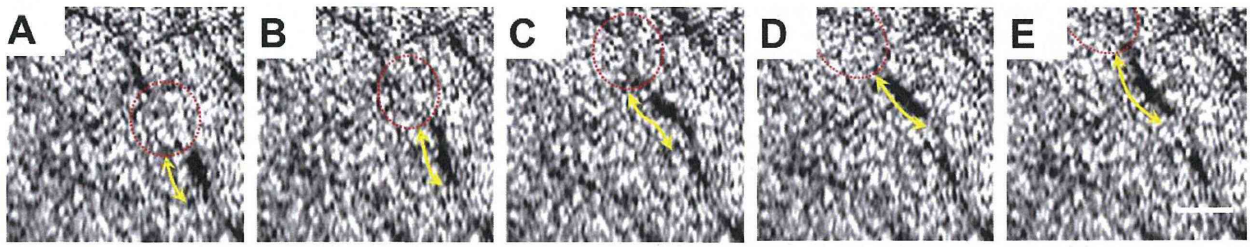

FIGURE 4. Dark tail elongation. The images show five consecutive frames with a bright particle (*dotted red circles*) and dark tail (*yellow, two-headed arrows*) flowing closely behind the bright particle in the parafoveal capillaries, which might correspond to leukocytes and erythrocyte aggregates, respectively. *Scale bar*: 100 μm. As the bright particles moved forward, the dark tails followed closely. The lengths of the dark tails became longer in a time-dependent manner, as shown by the *yellow arrows*.

Investigative Ophthalmology & Visual Science

TABLE. Characteristics of Subjects and Dark Tails

Subject	Sex	Age	Blood Pressure, mm Hg	Blood Data		Eye	Axial Length, mm	Average Velocity, mm/s	Average Dark Tail Length, μm			Average Dark Tail Elongation Rate	Average Vessel Diameter, μm
				RBC, $\times 10^4/\mu L$	Hb, g/dL				Zone a	Zone b	Zone c		
A	M	35	100/61	498	15.2	OD	26.2	1.14 ± 0.25	93.7 ± 53.5	119.7 ± 51.3	144.6 ± 42.4	0.54 ± 0.31	9.7 ± 0.3
B	F	42	98/61	415	12.7	OD	24.5	1.62 ± 0.30	61.9 ± 22.1	77.5 ± 20.0	95.3 ± 15.8	0.34 ± 0.27	8.7 ± 1.2
C	F	31	104/70	454	14.3	OD	25.1	1.48 ± 0.25	90.5 ± 20.9	144.0 ± 40.8	174.4 ± 56.5	0.54 ± 0.26	9.1 ± 0.9
D	F	23	103/64	428	13.5	OS	23.6	1.48 ± 0.28	75.7 ± 41.0	108.1 ± 42.0	135.3 ± 45.9	0.54 ± 0.22	13.0 ± 4.5
E	F	34	101/70	436	13.5	OD	24.7	1.22 ± 0.33	52.9 ± 35.2	98.7 ± 40.1	149.1 ± 47.5	0.55 ± 0.25	10.2 ± 0.4
F	M	38	107/71	500	15.5	OS	23.8	1.77 ± 0.54	86.7 ± 18.2	113.2 ± 34.2	142.1 ± 33.4	0.39 ± 0.23	10.4 ± 1.0
G	M	33	135/78	500	13.8	OD	26.3	1.58 ± 0.32	109.7 ± 35.3	150.1 ± 51.3	180.5 ± 63.5	0.74 ± 0.72	12.0 ± 0.9
H	M	40	110/64	479	14.5	OD	24.9	1.60 ± 0.34	84.1 ± 24.0	107.4 ± 23.4	135.4 ± 45.2	0.59 ± 0.56	12.2 ± 2.5
I	M	28	120/74	508	14.3	OD	27.1	1.53 ± 0.35	83.3 ± 36.8	121.3 ± 26.6	151.5 ± 32.9	0.48 ± 0.30	12.4 ± 2.0
J	F	22	102/46	522	15.7	OD	25.9	1.51 ± 0.21	73.1 ± 28.9	88.7 ± 29.1	114.2 ± 39.8	0.37 ± 0.17	11.8 ± 1.1
Mean ± SD		32.6 ± 6.7					25.2 ± 1.1	1.49 ± 0.36	81.2 ± 35.1	112.9 ± 41.4	142.2 ± 48.2	0.51 ± 0.37	11.0 ± 2.3

RBC, red blood cells; Hb, hemoglobin; OD, right eye; OS, left eye.

and c were 81.2 ± 35.1, 112.9 ± 41.4, and 142.2 ± 48.2 μm, respectively (Table). The length of the dark tails became longer in a time-dependent manner ($P < 0.0001$) (Figs. 4, 7A). The lengths of all dark tails were longer at zone c than at zone a. The overall average elongation rate was 0.51 ± 0.37, ranging from 0.02 to 1.87. Although the velocity of the dark tail was considerably slower when the length of the dark tail was longer, the elongation rate was not correlated with the velocity ($P = 0.56$, $r = -0.062$). The reproducibility of the dark tail elongation measurements was calculated by using ICC, and the obtained ICC value was 0.954.

Capillary Diameter

The mean capillary diameter in the parafovea was 11.0 ± 2.3 μm, with a range of 7.5 to 19.1. The diameters of the zones were not significantly different ($P = 0.43$) (Fig. 7B). A significant correlation was not found between diameter and velocity ($P = 0.31$, $r = 0.109$), between diameter and elongation rate ($P = 0.80$, $r = 0.027$), or between diameter and the length of the dark tail ($P = 0.15$, $r = -0.153$), suggesting that dark tail elongation was not caused by the gradual narrowing of the capillary lumen from upstream to downstream of blood flow.

DISCUSSION

In this study, we applied the AO-SLO system to monitor erythrocyte aggregates in healthy human retinas and demonstrated the phenomenon of erythrocyte aggregate elongation in the parafoveal capillaries for the first time. Careful observation of AO-SLO images revealed the pairing of a bright particle and a dark region flowing in the parafoveal capillaries (Fig. 4 and Supplementary Movie S1), which correspond to leukocytes and erythrocyte aggregates, respectively, as previously reported.[24] Their velocities and changes in length were clearly depicted in the spatiotemporal images; the dark bands, which were represented geometrically in the spatiotemporal images and corresponded to the dark tail trajectories, had a triangular or trapezoidal shape. Dark tail elongation was demonstrated by analyzing these shapes in all dark bands.

All of the dark tails showed elongation, but not shortening. Because all samples were recorded in healthy young subjects, elongation may be a physiological phenomenon that is observed normally in the human retina. Unfortunately, the mechanism of this phenomenon remains unknown because we could not finely visualize the elongating dark tail at a cellular level in the current study. However, we believe that dark tail elongation was caused by the packed erythrocytes that could not overtake the slow-moving leukocytes in the capillary lumen, thereby strongly blocking the imaging light of AO-SLO.[29] To eliminate the influence of vessel diameter difference on dark tail elongation, that is, influence on the moving object in the tapering lumen, which would be stretched and elongated, we evaluated the diameter uniformity of target vessels by dividing the vessels into thirds and measuring the diameter of each zone. The average diameter of the target vessels was 11.0 ± 2.3 μm, and significant differences were not found among the diameters of each zone ($P = 0.43$). Moreover, a significant association was not observed between the average diameter of the target vessel and the elongation rate ($P = 0.80$). These findings support the notion that dark tail elongation was not caused by the tapering lumen of vessels during the flow and that dark tail elongation would be induced by blood cell kinetics. Leukocytes might interfere with the flow of erythrocytes and induce packing of sequential erythrocytes, resulting in the detection of elongat-

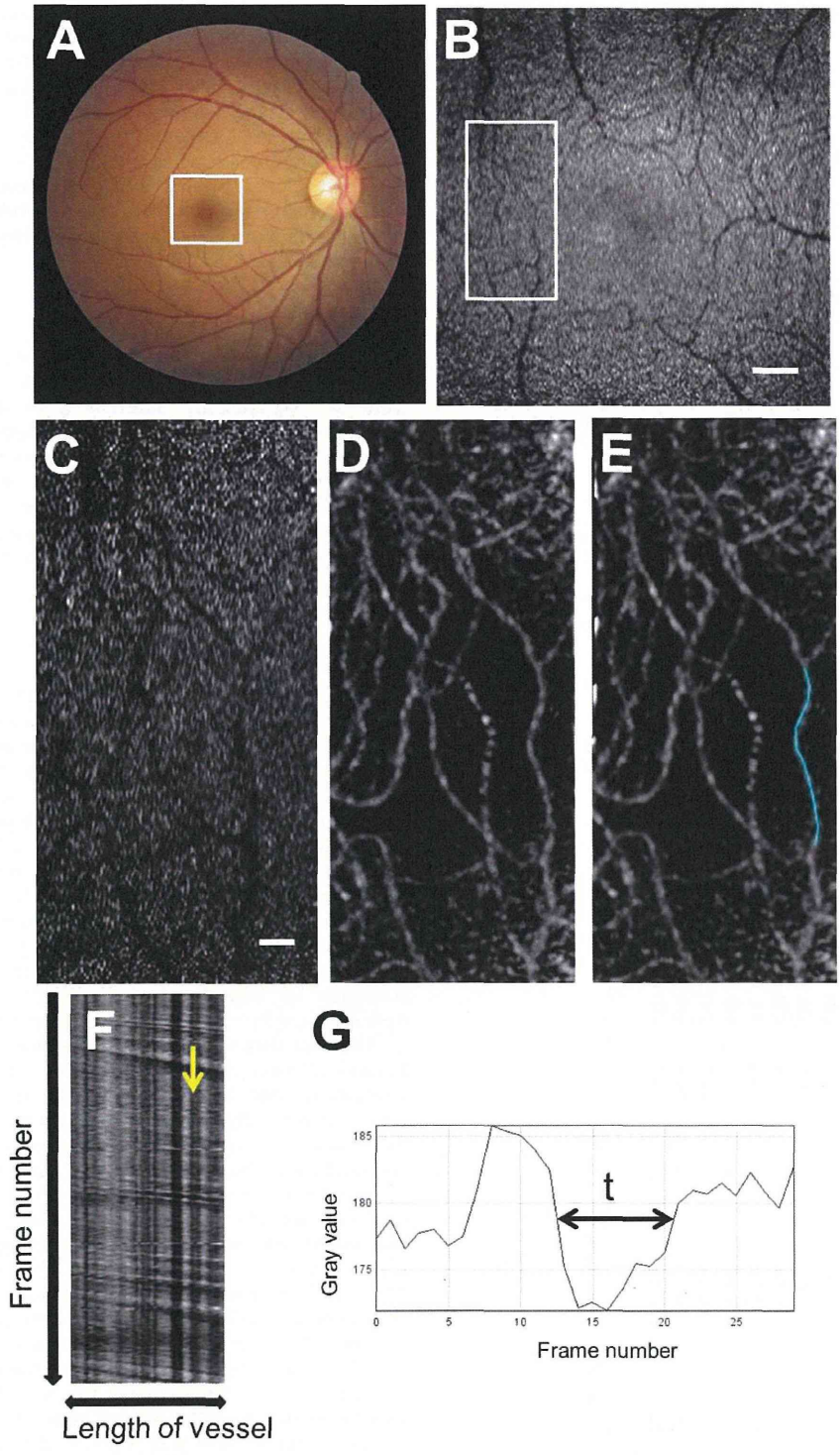

FIGURE 5. Dark tail analysis. (**A**) Color fundus photograph. (**B**) The AO-SLO image corresponds to the *outlined area* in (**A**). *Scale bar*: 200 μm. (**C**) The first frame of the AO-SLO video recorded in the *outlined area* in (**B**). *Scale bar*: 50 μm. The numerous *white dots* represent cone photoreceptors, and the *dark lines* represent the shadows of the parafoveal capillaries on the photoreceptors. (**D**) Constructed image of the capillaries. (**E**) The target vessel with dark tail flow was selected from one branch to another to ensure that they were free of another bifurcation (*blue line*). (**F**) A spatiotemporal image generated from the AO-SLO video by reslicing the frames along the line set on the target vessel (*blue line* in [**E**]) showing a white band paired with a dark band, which correspond to the trajectories of bright moving objects and dark tails, respectively. (**G**) Plot profile of the *yellow line* set on (**F**). The frame number of the gray value range that was lower than the averaged gray value (t) was measured as the time required for the dark tail to pass the point on the target vessel. The grayscale ranged from 0 (*black*) to 255 (*white*).

Investigative Ophthalmology & Visual Science

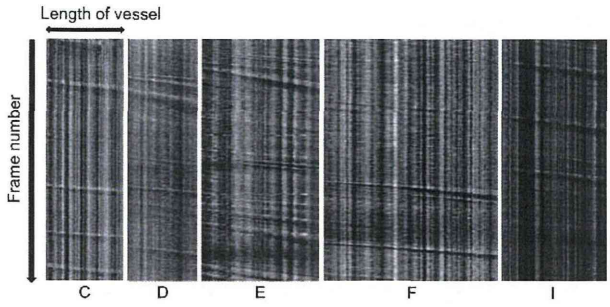

FIGURE 6. Examples of spatiotemporal images with dark tails. The letters for each image represent the subjects described in the Table. All examples show several dark bands that correspond to the trajectories of dark tails and are narrowest upstream and broadest downstream, indicating gradual elongation of dark tails.

ing dark tails closely behind the bright moving objects known as leukocytes in AO-SLO videos.[24]

It is widely accepted that erythrocytes play an extremely important role in determining the flow properties of blood.[44] Changes in the condition of erythrocytes cause impairment in microcirculation. To clarify microcirculation in diseases, erythrocyte aggregation has been used as a surrogate marker through analysis of the collected blood samples of patients. For example, increased erythrocyte aggregations were reported to be cardiovascular risk factors in patients with diabetes mellitus.[45] Erythrocyte aggregation was also increased in patients with SLE, causing a decreased flow that might contribute to the thromboembolic process.[5] In patients with Behçet's disease, increased erythrocyte aggregates are related to increased fibrinogen, but not to thrombosis and uveitis.[32] These findings motivated us to measure the dark tail velocity and the elongation of dark tail length to analyze the dynamics of erythrocyte aggregates in parafovea capillaries. Although a few studies have reported direct and noninvasive observation of erythrocyte aggregation using conjunctival blood vessels,[33] to the best of our knowledge, this is the first study to report noninvasive and direct monitoring of erythrocyte aggregates in human retinal capillaries and the phenomenon of erythrocyte aggregate elongation. In the future, the measurement of dark tail length or elongation rate will be tested in various diseases using methods that are similar to those described in this study, and their clinical importance will be investigated.

The peculiarity of AO-SLO is the correction of ocular lower- and higher-order aberrations, enabling noninvasive observation of each retinal layer, including the photoreceptor layer,[24] nerve fiber layer,[46] and capillary layer,[34] under high resolution. Although the aim of this study was to analyze blood cells, the scanning layer of AO-SLO was focused on the photoreceptor layer rather than the capillary layer, and blood cells were observed as shadings on the shadows of the bright cone mosaic patterns of photoreceptors. As previously reported, the reflected light characteristics of the AO-SLO laser from photoreceptors is affected by blood cells because of their differences in scattering coefficients.[24,47] When the scanning layer is focused on the photoreceptor layer, leukocytes are candidates for the bright particles moving in the dark vessel shadows due to the low absorptivity of the AO-SLO laser, resulting in detection of leukocytes as background illumination of photoreceptors. Blood plasma is another bright particle candidate, but its signal is slightly weaker than that of leukocytes.[24,41] Conversely, erythrocytes are strong candidates for the region that is darker than the vessel shadow because they block the AO-SLO lasers, and their aggregation is thought to be a dark tail. Because these differences in the shades on the photoreceptor layer help to distinguish blood components in the retinal microvasculature, we believe that the best focus for monitoring erythrocyte aggregation is the photoreceptor layer (Supplementary Movie S2). Meanwhile, only the numerous high-intensity particles that may correspond to a mixture of reflected light from erythrocytes and from the retinal layers near the capillary layer can be observed when the scanning layer is focused on the capillary layer, and a distinction between blood components is impossible with the accuracy of the current confocal optic system (Supplementary Movie S3).

Detection of a pair of bright particles and a dark tail flowing in the retinal circulation using AO-SLO bears a remarkable resemblance to the perception of a bright moving object and its dark tail under blue field entoptic phenomenon; this type of physiological phenomenon is perceived as numerous bright particles that move in a flowing manner with a synchronous rhythmic acceleration that corresponds to the cardiac cycle against bright, diffuse illumination.[15] Sinclair et al. suggested that leukocytes are the source of the bright particles perceived under the blue field entoptic phenomenon and that erythrocytes are detected as dark particles using animal preparations; that is, the entoptic images are the perception of the gaps between erythrocytes created by leukocytes, which have large cell bodies.[15] Erythrocyte aggregates have also been observed in retinal circulation in studies that used scanning laser ophthalmoscopy with fluorescein angiography. These studies suggested that the dark (hypofluorescent) spots detected in the stained capillaries were rouleaux formations of erythrocytes and represented erythrocyte aggregates. The fluorescein characteristics showed that the hemoglobin and oxyhemoglobin absorption bands were clearly visible in the fluorescence

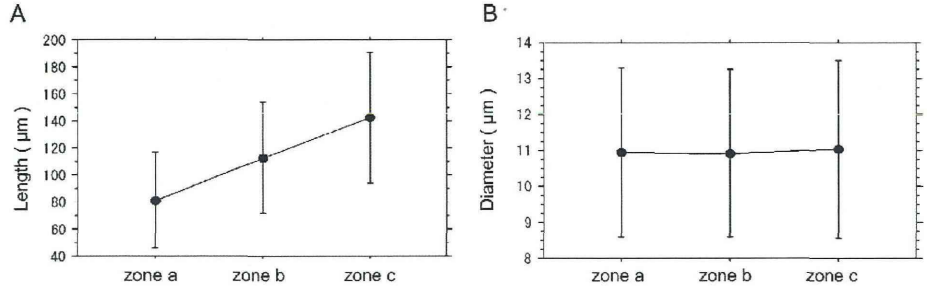

FIGURE 7. Differences in dark tail length and capillary diameter among three zones. Target vessels were separated into three zones from upstream to downstream of blood flow (zones a, b, and c) in order to evaluate the time-dependent change in dark tail length. (**A**) Significant differences in the dark tails were found among zones a, b, and c. The dark tails became longer in a time-dependent manner ($P < 0.0001$). (**B**) The diameters of the target vessels were not significantly different among the three zones ($P = 0.43$), suggesting that dark tail elongation is not caused by the gradual narrowing of the capillary lumen from upstream to downstream of blood flow.